Iterative time-reversal for multi-frequency hyperthermia

(article starts on next page)

Physics in Medicine & Biology

IPEM Institute of Physics and Engineering in Medicine

CrossMark

PAPER

Iterative time-reversal for multi-frequency hyperthermia

Massimiliano Zanoli (ORCID) **and Hana Dobšíček Trefná** (ORCID)

Dept. Electrical Engineering, Chalmers University of Technology, Gothenburg, SE, Sweden

E-mail: hanatre@chalmers.se

Abstract

Time-reversal (TR) is a known wideband array beam-forming technique that has been suggested as a treatment planning alternative in deep microwave hyperthermia for cancer treatment. While the aim in classic TR is to focus the energy at a specific point within the target, no assumptions are made on secondary lobes that might arise in the healthy tissues. These secondary lobes, together with tissue heterogeneity, may result in hot-spots (HSs), which are known to limit the efficiency of the thermal dose delivery to the tumor. This paper proposes a novel wideband TR focusing method that iteratively shifts the focus away from HSs and towards cold-spots from an initial TR solution, a procedure that improves tumor coverage and reduces HSs. We verify this method on two different applicator topologies and several target volume configurations. The algorithm is deterministic and runs within seconds, enabling its use for real-time applications. At the same time, it yields results comparable to those obtained with global stochastic optimizers such as Particle Swarm.

1. Introduction

In deep microwave hyperthermia (MW-HT) for cancer treatment, a conformal array of antennas, called applicator, is used to non-invasively and selectively increase the temperature of a deep-seated tumor up to $40\,^\circ$C–$44\,^\circ$C for approximately one hour (Elming *et al* 2019, Paulides *et al* 2020). Randomized clinical trials have demonstrated the efficacy of this technique in enhancing the therapeutic effects of chemo- and radio-therapy (Cihoric *et al* 2015, Datta *et al* 2015, 2016). The challenge in MW-HT is to reach deep-seated targets with adequate power deposition while keeping the nearby healthy tissues (HSs) below a safety temperature threshold. These HSs lie in the path between the antenna and the target, and they tend to absorb energy from the traveling wave, as a consequence of their relatively high conductivity at RF frequencies. The power loss in these tissues can cause hot-spots (HSs), which effectively limit the maximum temperature achievable in the target. This can prevent the treatment from reaching high therapeutic thermal doses (Paulides *et al* 2010, Kok *et al* 2017). Superficial HSs within depths of one to two centimeters from the skin can be suppressed by applying a water bolus circulated with cool water. Other HSs might arise deeper in the body due to the anatomical heterogeneity and interfaces between tissues with different dielectric properties, together with the imperfect interference pattern generated by the phased array. In such cases, the pattern has to be improved by means of amplitude and phase steering of the applicator array, with parameters obtained by a hyperthermic treatment planning (HTP) step (Gavazzi *et al* 2020).

Several methods for determining the optimal amplitudes and phases for an applicator array yielding satisfying target coverage and limited HS temperatures have been developed in the past and are still subject of ongoing research (Paulides *et al* 2013, Kok *et al* 2015). These methods can be classified into two main categories: specific absorption rate (SAR) based and temperature (*T*) based. SAR based techniques rely on the assumption that the SAR distribution is predictive of the temperature distribution in the patient (Canters *et al* 2009). However, since the thermal response of the body can be highly nonlinear, SAR-based optimizers can yield sub-optimal, while still clinically relevant, HTP parameters. *T*-based optimizers, on the other hand, have evolved to include complex nonlinear aspects such as discrete vasculature and systemic response under thermal stress (Kok *et al* 2013). Ideally, a full implementation of *T*-based HTP in the clinical routine is desirable, since temperature is
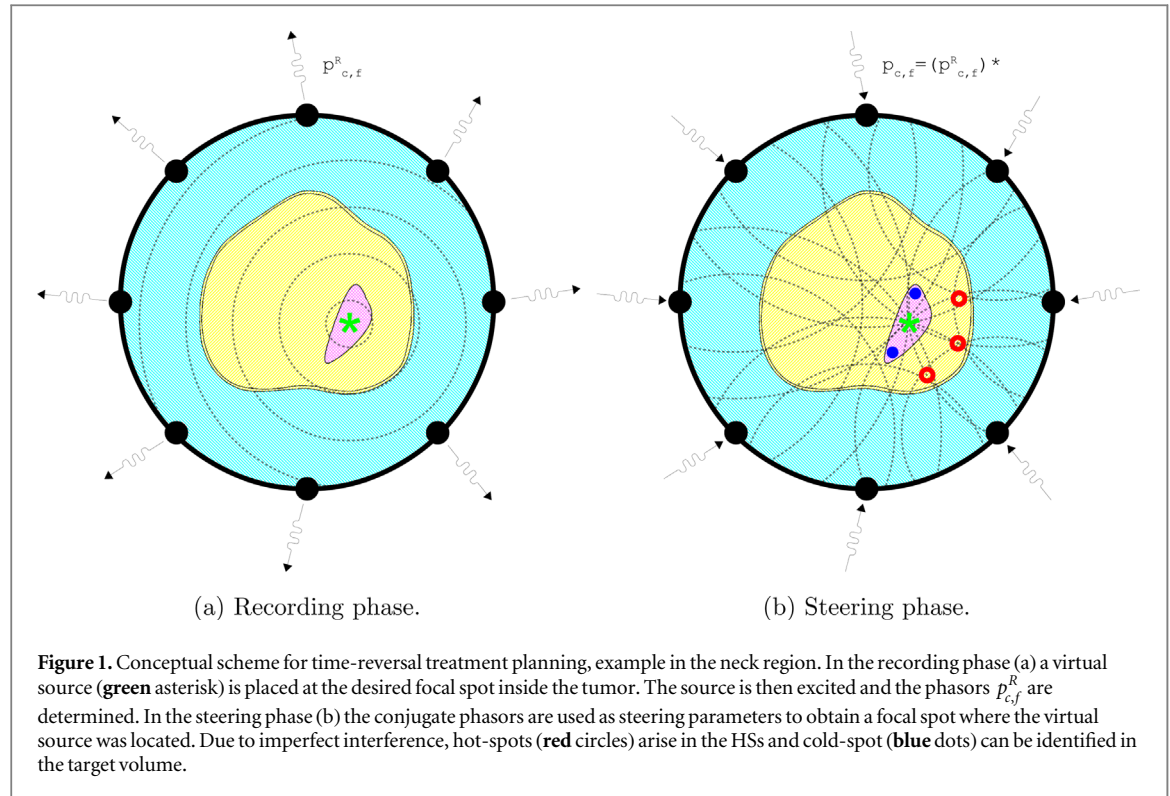
the objective dose. In current practice, however, the theoretical benefits of T-based HTP are somewhat diminished due to the lack of accurate estimations of the thermal tissue properties (De Greef *et al* 2010, Canters *et al* 2012, 2013). Such thermal properties, and blood perfusion in particular, exhibit large variations across patients and even at individual level in different treatment sessions. Therefore, both SAR-based and T-based approaches are being clinically applied as both require adjustments during treatment in response to hot spots (Rijnen *et al* 2013, Kok *et al* 2017). Considering the current equivalence of these two approaches, in the present work we consider only SAR based HTP techniques.

Among them, the eigenvalue (EV) and, more recently, the particle swarm (PS) algorithms have become the most established in the literature (Paulides *et al* 2013, Kok *et al* 2015). The EV method maximizes the ratio between the average SAR in the target and in the remaining tissues (Böhm *et al* 1993, Bardati *et al* 1995). When the resulting temperature distribution is showing overheated healthy regions, a weighing factor can be introduced to iteratively reduce the power deposition at those locations (Köhler *et al* 2001). EV is a direct method that provides a fast and deterministic solution, but its main limitation lies in the form of the cost function, which has to be a quadratic ratio between polynomials. Quadratic cost function predictions have been shown to correlate poorly with the SAR or temperature rise in the tumor target volume during clinical treatment (Canters *et al* 2009). For this reason, more clinically relevant and temperature-predicting indicators such as the hotspot-to-target quotient (HTQ) have been proposed (Canters *et al* 2010). Since the evaluation of the HTQ involves at least one nonlinear step with respect to the complex array steering parameters, EV cannot be directly used to determine the HTQ-optimal solution. A second limitation of EV occurs with multi-frequency optimization: the generalized EV form can not be defined for multiple simultaneous operating frequencies in a conjoint manner (Trefná *et al* 2017, Zanoli and Trefná 2020).

There is mounting evidence that the development of UWB applicators capable of operating at different frequencies will lead to improved target coverage and HS suppression (Converse *et al* 2006, Trefná *et al* 2010a, Bellizzi *et al* 2017, Kuehne *et al* 2020). An UWB system can exploit the complementary interference patterns generated by different frequencies to increase the net average power delivered to the tumor while reducing the absorption in HSs. The benefit of UWB is even more pronounced for the treatment of tumors in challenging locations, such as the brain (Winter *et al* 2015, Takook *et al* 2018). The brain region is in fact characterized by a combination of anatomical and physiological factors that require an extra degree of accuracy in the formation of the heating pattern. The cerebral tissue is more sensitive to deviations in temperature than other tissues (Yarmolenko *et al* 2011), and the presence of cerebrospinal fluid causes strong HSs to appear in the immediate vicinity of the brain (Schooneveldt *et al* 2019). The single-frequency constraint of EV might therefore represent an insurmountable limitation for multi-frequency HTP.

PS is another type of HTP optimizer used in clinical practice (Paulides *et al* 2013). If the PS optimization is configured to minimize the HTQ, the resulting steering settings can exhibit significant differences from those given by EV. In particular, the resulting raw power deposition ratio might be worse than the one obtained via EV, but the SAR distribution is often better in terms of more relevant clinical parameters: target coverage and heating homogeneity. Furthermore, the PS method can easily be extended for use with multiple operating frequencies. The drawback with PS, being a stochastic algorithm, is its long execution time needed to consistently converge to the same global optimum between different executions. A typical run with 100 iterations, as usually required for reasonable accuracy, can take half an hour or more to complete, depending on the model resolution.

Time reversal (TR) focusing is a fast, intrinsically wide-band and deterministic method that has been proposed and validated as an alternative microwave HTP technique (Guo *et al* 2005, Trefná *et al* 2010b). TR processing is a well characterized inverse filter initially developed for focusing ultrasound pulses generated by transducer arrays inside a biological target (Thomas and Fink 1996, Fink *et al* 2004), and subsequently extended for use with electromagnetic antenna arrays (Lerosey *et al* 2004). It exploits the time and space reciprocity of the wave equation to determine the optimal phase and amplitude settings of an array of radiators that will cause the highest constructive interference to occur at the desired location. In its basic implementation, with a single virtual source placed at the center of the tumor, TR already exhibits improved target coverage and HTQ than EV (Trefná *et al* 2010a, 2010b, Takook *et al* 2015), though not comparable to PS optimization. Further improvements for HS-management in TR have been proposed for high-intensity focused ultrasounds (HIFU), based on iterative methods (Leduc *et al* 2012). In general, the major hindrance for the clinical introduction of TR-based HTP is its limited ability to suppress HSs. In this work, we present a novel deterministic HS suppression algorithm for TR-based HTP that yields results comparable to those obtained via global PS optimization, while being significantly faster. The rest of the paper is organized as follows: we first introduce the iterative procedure in detail, to later benchmark its performances numerically for two different applicator array topologies: a collar for tumors in the neck and a helmet for tumors in the brain. For the neck model, we further consider different target locations and sizes, to assess the algorithm's robustness to different scenarios. For each test case, HTP quality and performance indicators are computed and compared against those obtained with EV, PS and classic TR.

Figure 1. Conceptual scheme for time-reversal treatment planning, example in the neck region. In the recording phase (a) a virtual source (**green** asterisk) is placed at the desired focal spot inside the tumor. The source is then excited and the phasors $p^R_{c,f}$ are determined. In the steering phase (b) the conjugate phasors are used as steering parameters to obtain a focal spot where the virtual source was located. Due to imperfect interference, hot-spots (**red** circles) arise in the HSs and cold-spot (**blue** dots) can be identified in the target volume.
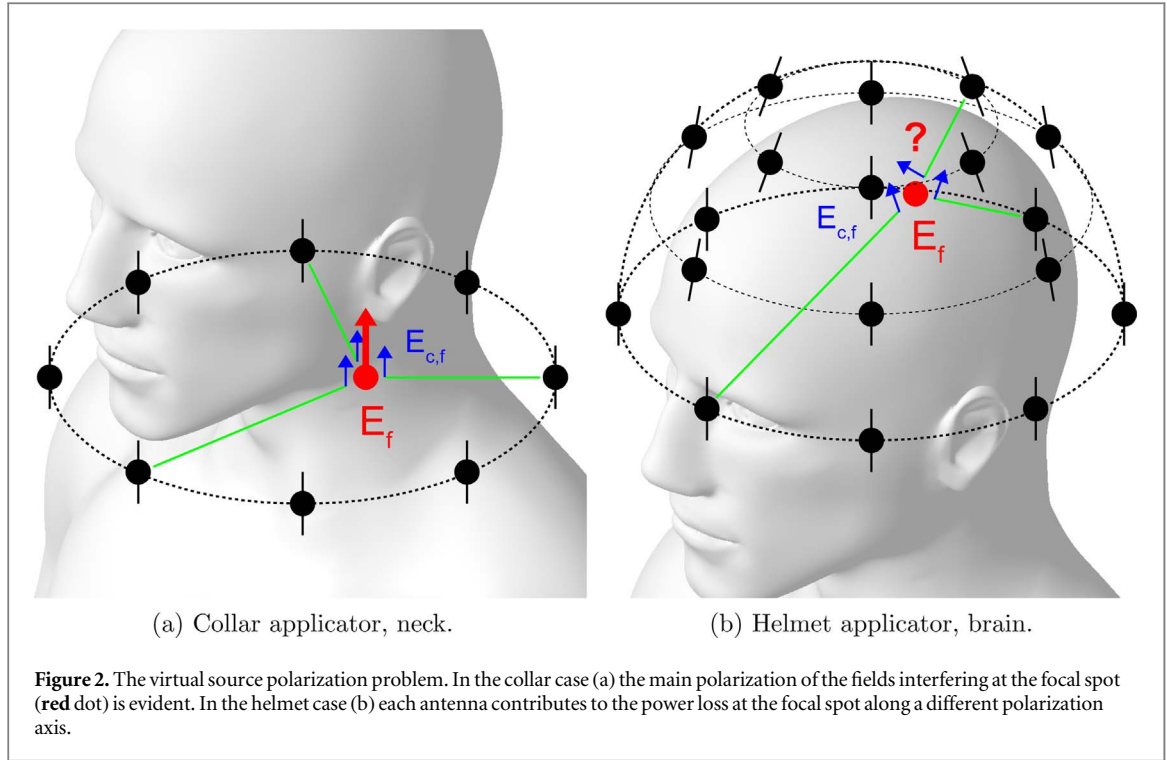
2. Theory

2.1. Classic TR focusing

TR focusing is achieved by placing a so-called *virtual source* at the desired focal spot and by recording the impulse response at the antenna locations (figure 1(a)). The recorded signals are then back-propagated simultaneously by all the antennas, generating an interference pattern that exhibits full phase coherence at the original source location (figure 1(b)). Together with the desired peak, however, secondary lobes appear due to both the limited aperture of the array and the anatomy of the patient. In the frequency domain, the TR operator corresponds to a complex conjugation (*):

$$p_c(f) = [p^R_c(f)]^*, \tag{1}$$

where p^R_c is the complex phasor recorded by the array channel c at frequency f during source excitation, while p_c is the complex steering parameter for the same channel to focus at the source location. Under this perspective, a discrete set of simultaneous operating frequencies can be selected for treatment, rather than wideband pulses. In practice, an applicator can be operated to switch between single frequencies in finely interleaved time slots, if the duration of each slot is small compared to the biological response (Trefná *et al* 2017). This simplifies the complexity of the hardware needed for feeding the HT applicator (Trefná *et al* 2012). The rest of the analysis will therefore be carried out assuming that n_f simultaneous operating frequencies can be independently controlled in phase and amplitude for each of the n_c channels of the array applicator.

TR focusing requires in principle only one EM simulation per virtual source, which makes it attractive in terms of computational resources. Unfortunately, this single simulation is not sufficient to assess the quality of the resulting treatment planning. The HTP quality indicators must in fact be evaluated over the focused SAR distribution (figure 1(b)). Moreover, since the immediate TR solution for HTP might not be optimal or clinically viable, further adjustments might be needed, which would require additional simulations. In view of this, it is more convenient to run a separate simulation for each antenna/channel c in the array, as is the case for EV or PS. The TR solution at any point can then be determined from this set of E-field distributions via a generalized and source-free TR method described later in section 2.2. Denoting with ^{t} the transpose operation (without conjugate), the complex E-field distributions and steering parameters relative to all channels at a certain frequency can be joined into column vectors for compactness:

$$\boldsymbol{p}_f = [p_{1,f} \ p_{2,f} \ ... \ p_{n_c,f}]^t \qquad \boldsymbol{E}_f = [E_{1,f} \ E_{2,f} \ ... \ E_{n_c,f}]^t. \tag{2}$$

Figure 2. The virtual source polarization problem. In the collar case (a) the main polarization of the fields interfering at the focal spot (**red** dot) is evident. In the helmet case (b) each antenna contributes to the power loss at the focal spot along a different polarization axis.

2.2. Challenges for TR focusing in MW-HT

A number of challenges arise when implementing TR as HTP. First of all, the choice of the source location, or focal spot. Intuitively, the source should be placed at the center of the tumor, but this is often hard to define, especially for irregular shapes. The center of mass of the tumor can be picked as an initial guess, but this choice often leads to inhomogeneous or insufficient heating of deep or peripheral tumor areas. Cold-spots in the target volume should be avoided, as they reduce the treatment's efficacy. Better coverage can be achieved, for example, by translating the focal spot progressively towards the internal, deeper part of the target volume (Takook *et al* 2017). Second, HSs arising in healthy tissues must be suppressed, to allow a higher deposition in the target. In order to shift the focus away from these locations, the natural approach under the TR perspective would be to place secondary sources, record their impulse response, and subtract these secondary solutions from the primary one. Taken together, these considerations suggest that an initial TR solution with source at the tumor center can be iteratively improved by shifting the set of complex steering parameters away from HSs and towards cold-spots.
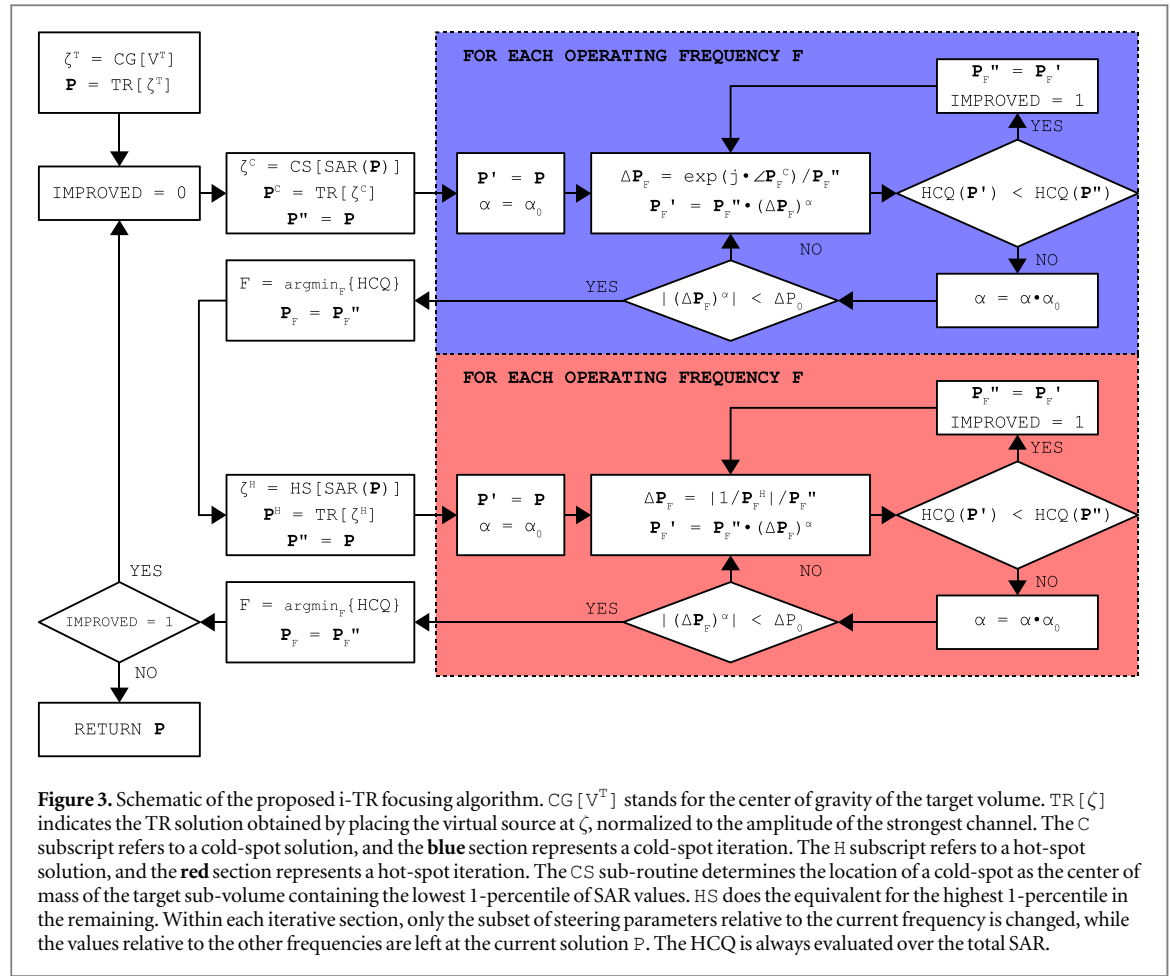
A second aspect of TR focusing is the choice of the polarization axis for the virtual source. The polarization problem in vector field focusing has been addressed in several ways in the literature, also recently (Iero *et al* 2016, Battaglia *et al* 2020). In the case of a cylindrical applicator, the antennas can be aligned to the symmetry axis (figure 2(a)): the virtual source should then also be aligned with this principal axis. In more complex array topologies such as a semi-spherical helmet, the E-field generated by each antenna can vary significantly in polarization, depending on the location of the focal spot (figure 2(b)). The resulting interference is no longer characterized by a single main polarization, and the concept of virtual source becomes inadequate. This concept should then be dropped in favor of the more generalized concept of complex power contribution at the focal spot. We know that the SAR at a location ζ resulting from the superposition of all channel fields at a particular frequency f is given by:

$$\text{SAR}_f(\zeta) = \frac{1}{2} \frac{\sigma_f(\zeta)}{\rho(\zeta)} \boldsymbol{p}_f^{*\,t} \langle \boldsymbol{E}_f^*(\zeta), \boldsymbol{E}_f^t(\zeta) \rangle \boldsymbol{p}_f, \tag{3}$$

where $\langle \cdot, \cdot \rangle$ denotes the scalar product, while σ_f and ρ are the local material conductivity (frequency-dependent) and density, respectively. The outer product, called SAR *matrix* and denoted $\boldsymbol{Q}_f$, contains information about the complex SAR contributions from each channel irrespective of their polarization directions:

$$\boldsymbol{Q}_f = \frac{1}{2} \frac{\sigma_f}{\rho} \langle \boldsymbol{E}_f^*, \boldsymbol{E}_f^t \rangle$$

$$\langle \boldsymbol{E}_f^*, \boldsymbol{E}_f^t \rangle = (\boldsymbol{e}_f^X)^* (\boldsymbol{e}_f^X)^t + (\boldsymbol{e}_f^Y)^* (\boldsymbol{e}_f^Y)^t + (\boldsymbol{e}_f^Z)^* (\boldsymbol{e}_f^Z)^t, \tag{4}$$

where a Cartesian coordinate system has been assumed. By construction, $\boldsymbol{Q}_f$ is Hermitian and positive semi-definite. This property allows us to perform an inverse operation and decompose $\boldsymbol{Q}_f$ into an outer product, such

Figure 3. Schematic of the proposed i-TR focusing algorithm. `CG[V^T]` stands for the center of gravity of the target volume. `TR[ζ]` indicates the TR solution obtained by placing the virtual source at ζ, normalized to the amplitude of the strongest channel. The `C` subscript refers to a cold-spot solution, and the **blue** section represents a cold-spot iteration. The `H` subscript refers to a hot-spot solution, and the **red** section represents a hot-spot iteration. The `CS` sub-routine determines the location of a cold-spot as the center of mass of the target sub-volume containing the lowest 1-percentile of SAR values. `HS` does the equivalent for the highest 1-percentile in the remaining. Within each iterative section, only the subset of steering parameters relative to the current frequency is changed, while the values relative to the other frequencies are left at the current solution P. The HCQ is always evaluated over the total SAR.

that:

$$Q_f = \hat{p}_f^* \hat{p}_f^t, \tag{5}$$

where $\hat{p}_f$ is a column vector containing the complex contribution of every channel at ζ. The solution $\hat{p}_f$ of the decomposition can be obtained as the only non-singular eigenvector of Q_f. The sought set of steering parameters for focusing at ζ in a generalized TR perspective is the complex conjugate of this solution:

$$p_{c,f} = \hat{p}_{c,f}^*. \tag{6}$$

2.3. Iterative time-reversal

The proposed iterative TR (i-TR) focusing technique takes into account all the points discussed above to improve an initial TR solution for HTP. The schematic of the procedure is shown in figure 3. The initial solution p is found at the center of mass of the tumor using equation (6). The resulting SAR distribution is analyzed and the most prominent cold-spot is identified as the center of mass of the contiguous sub-volume containing the lowest 1-percentile of SAR within the target volume. The TR solution at the cold-spot is calculated and the iterations begin for one frequency at a time, shifting the *phase* of the current parameter set *towards* that of the cold-spot solution p^C.

The iterative section aims at minimizing a novel cost function specifically tailored for i-TR, which we will call the *hot-to-cold spot quotient* (HCQ), defined as:

$$\text{HCQ} = \frac{\overline{\text{SAR}}_{\text{R1}}}{\overline{\text{SAR}}_{\text{T1}}}, \tag{7}$$

where $\overline{\text{SAR}}_{\text{R1}}$ is the average SAR in the sub-volume of remaining HSs containing the highest 1-percentile of SAR values, while $\overline{\text{SAR}}_{\text{T1}}$ is the equivalent for the lowest 1-percentile in the target volume. The individual frequency iteration is carried out stepping by a geometrical factor α, with $0 < \alpha < 1$:

$$p_f' = p_f'' \cdot \Delta p_f^\alpha, \tag{8}$$

$$\Delta \boldsymbol{p}_f = \begin{cases} \left(e^{j \angle \boldsymbol{p}_f^C} \right) \big/ \boldsymbol{p}_f'', & \text{for cold-spot iteration} \\ \left(\left| 1 \big/ \boldsymbol{p}_f^H \right| \right) \big/ \boldsymbol{p}_f'', & \text{for hot-spot iteration} \end{cases}, \tag{9}$$

where j is the imaginary unit, and all operations are intended to be element-wise. The buffer variable $\boldsymbol{p}_f''$, initially set as $\boldsymbol{p}_f$, is replaced by the search direction $\boldsymbol{p}_f'$ only if the stepping was successful, i.e. if the resulting HCQ($\boldsymbol{p}'$) is better than the current HCQ($\boldsymbol{p}''$). Note that, while only the subset of steering parameters relative to one frequency is iterated at a time, the assessment of HSs, cold-spots and HCQ at each iteration is always carried out over the total SAR distribution:

$$\text{SAR} = \text{SAR}_1 + \text{SAR}_2 + ... + \text{SAR}_{n_f}. \tag{10}$$

If the stepping was not successfull, the step factor α is geometrically reduced and another attempt is made. If the norm of the step $|\Delta \boldsymbol{p}^\alpha|$ falls below a threshold value Δp_0 without any improvement on the HCQ, the next frequency is considered and iterated. Once all frequencies have been iterated, only the subset of parameters $\boldsymbol{p}_f$ relative to the frequency that yielded the best improvement in HCQ is updated with $\boldsymbol{p}_f''$.

A similar procedure is then carried out for the HS. The updated SAR distribution is analyzed and the most prominent HS is identified as the highest 1-percentile of SAR within the HSs. However this time the *amplitude* of the parameters is shifted *away from* the HS solution $\boldsymbol{p}^H$. If at least one spot iteration was successful in improving the HCQ, a new cold-spot is considered and iterated, and so on. Otherwise, the algorithm terminates.

The parameter Δp_0 is directly related to the desired precision on the steering parameters. We select a precision of 1% ($\Delta p_0 = 0.01$) since RF systems usually do not provide steering accuracy higher than ± 5 % (Wust *et al* 1998, Paulides *et al* 2007). The parameter α_0, on the other hand, decides the length of the first iterative step and its subsequent geometrical progression. As shown later in section 4.3, the value of α_0 affects mainly the algorithm's convergence speed and number of iterations, and has almost no effect on the overall accuracy. Its optimal value $\alpha_0 = 0.1$ is determined by means of a sensitivity analysis, and this value is kept throughout all executions reported here.

3. Method

We compare the proposed i-TR technique with EV, PS, and classic TR. The evaluation is carried out in two steps: we first assess the quality of the HTPs via SAR-based indicators, then validate them in terms of resulting thermal distributions. The test cases include 3 inhomogeneous artificial targets of increasing size in the neck region and 2 tumor-filled realistic targets, one in the neck and one in the brain. The thermal validation is carried out only for the realistic targets. The HTP methods are benchmarked in terms of the following quality indicators:

- HTQ: HS to target quotient, as defined in Canters *et al* (2010):

$$\text{HTQ} = \frac{\overline{\text{SAR}}_{R1}}{\overline{\text{SAR}}_T} \tag{11}$$

i.e. the ratio between the average SAR in the sub-volume containing the highest 1-percentile SAR among the remaining tissues ($\overline{\text{SAR}}_{R1}$) and the average SAR in the target volume ($\overline{\text{SAR}}_T$). Values of HTQ around or below 1 are typically considered for clinical treatment.
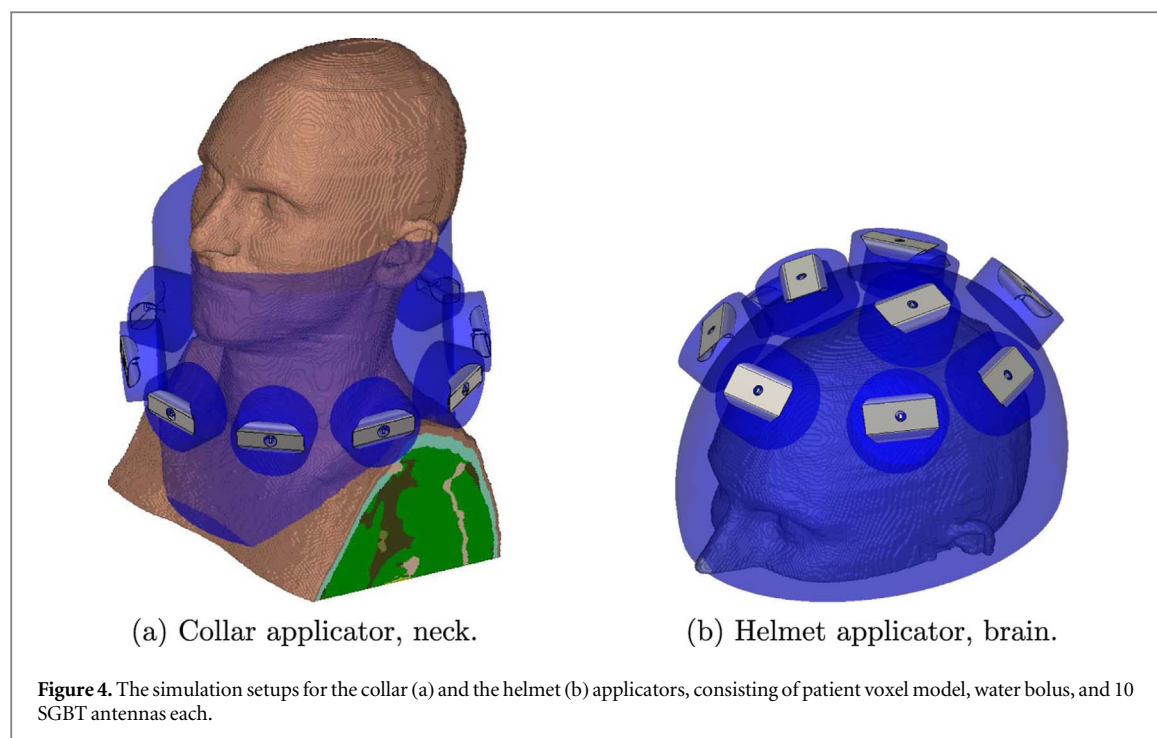
- TC_x: iso-SAR target coverage, as defined in Togni *et al* (2013):

$$\text{TC}_x = \frac{V_T(x)}{V_T}, \qquad V_T(x) \mid \text{SAR}[V_T(x)] \geqslant x \cdot \text{SAR}[V] \tag{12}$$

i.e. the fraction of the target volume V_T where SAR values are above a given fraction x of the SAR peak value in the whole patient volume V. Both the TC_x value and the fraction x are usually expressed as percentage, and the TC_x index is evaluated in this work for $x = 25\%$ or $x = 50\%$ depending on the model at hand. Values of TC_{25} greater than 75% are typically considered for clinical treatment.

Both the HTQ and TC indicators are evaluated over the 1g-averaged SAR distribution as detailed in section 3.3. The TR, i-TR, EV and PS focusing algorithms are all implemented in MATLAB® (The MathWorks Inc. 2019). Field processing steps are parallelized and executed in single precision on a high performance GPU (nVidia Quadro RTX 6000) where possible. We further evaluate the speed and computational cost of each method using the following metrics:

- *Running time*, t_r: time needed for the HTP optimization algorithm to complete, excluding SAR matrix preparations.

(a) Collar applicator, neck.   (b) Helmet applicator, brain.

Figure 4. The simulation setups for the collar (a) and the helmet (b) applicators, consisting of patient voxel model, water bolus, and 10 SGBT antennas each.

- *Number of evaluations*, n_e: how many times the cost function is evaluated by the algorithm (zero for EV and classic TR).

For the thermal validation, whose setup is detailed in section 3.4, the following HTP quality indicators are used to evaluate the resulting temperature distributions:

- *Cumulative histograms*: of the temperature distribution within the target.

- T_{50}: median temperature in the target volume, as defined in Fatehi *et al* (2007).

3.1. Applicator array topologies

The HTP algorithms are tested on two array topologies: cylindrical and semi-spherical. The cylindrical applicator (figure 4(a)) is meant for treatment of tumors in the neck region. It consists of 10 radiators arranged on one ring of 20 cm diameter. The radiators are self-grounded bow-tie antennas (SGBT), which work across the range 400–800 MHz and have been adapted specifically for ultra-wideband MW-HT (Takook *et al* 2017). A cylindrical water bolus, with average thickness 4 cm, is included between the antennas and the patient to improve matching. The SGBT antennas are further immersed each into a protruding cylindrical extension of the water bolus, to enhance their directivity and reduce cross-coupling between array elements.

The semi-spherical applicator (figure 4(b)) represents a simplified version of a helmet applicator for brain tumors. It consists of 10 SGBT antennas radially arranged from the top of the scalp and following the skull's curvature. The applicator covers only a small part of the head and, as such, can only be meaningfully used for targeting volumes close to the the skull. This applicator is not optimized for an effective treatment of deep-seated brain tumors, but it is intended for the investigation of the i-TR method's robustness to mixed polarization axes. The average water bolus thickness for this applicator is 1.5 cm.

3.2. Human model and target volumes

The *Duke* human voxel model from the IT'IS Foundation (Gosselin *et al* 2014) is used as virtual patient for both regional treatment plannings. The original resolution of $1 \times 1 \times 1$ mm is down-sampled to $2 \times 2 \times 2$ mm to spare computational resources. The constant (density) and dispersive (permittivity, conductivity) tissue properties are obtained from the IT'IS Foundation database (Hasgall *et al* 2012). A $230 \times 260 \times 390$ mm subset of the model is selected to represent the neck region, figure 4(a). The resulting voxel matrix includes 47 segmented tissues. For the brain applicator, a smaller subset is selected, $230 \times 260 \times 138$ mm, figure 4(b). The resulting voxel matrix includes 31 tissues.
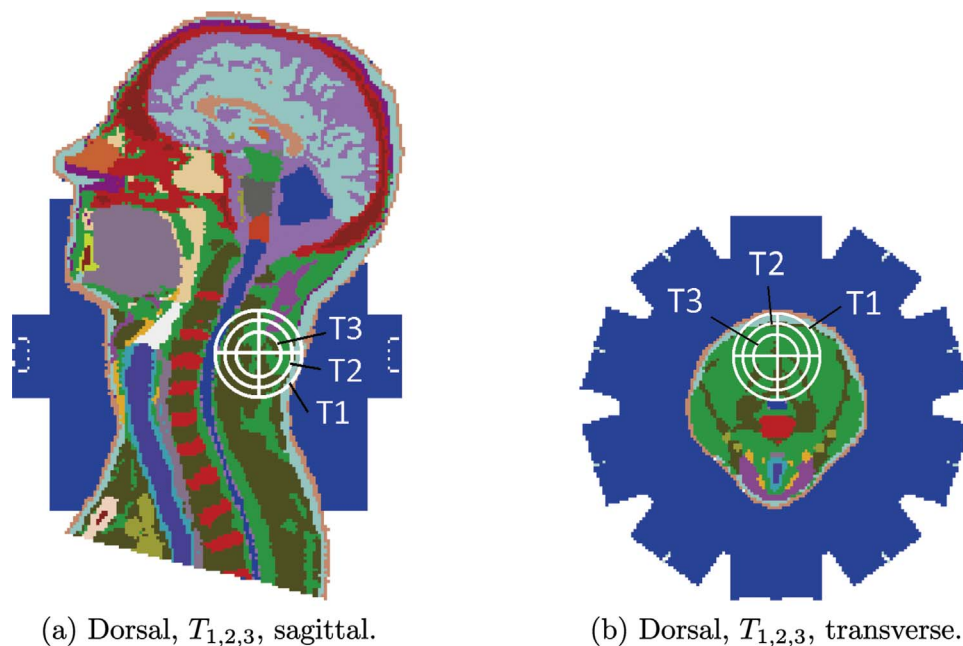
Figure 5. Artificial heterogeneous target volumes. The targets are spherical and concentric. They are delineated in **white**. The volume center is indicated with a cross. Sections are taken at the volume center.

Table 1. List of target volumes. The most relevant tissues within the target are reported in percent of volume. For the *artificial* targets: M is muscle, F is fat, O is other. For the *realistic* targets: X is mucous membrane, M is muscle, L is larynx, T is tendon ligament, C is cerebrospinal fluid, G is gray matter, W is white matter, S is skull, O is other.

Label	Region	Volume	Location	Topology	Composition
T_1	Neck	113 ml	Dorsal	Spherical	73% M, 18% F, 09% O
T_2	Neck	48 ml	Dorsal	Spherical	77% M, 21% F, 02% O
T_3	Neck	14 ml	Dorsal	Spherical	78% M, 22% F, 00% O
T_4	Neck	85 ml	Larynx	Concave	25% X, 20% M, 18% L, 13% T
T_5	Brain	30 ml	Meninges	Convex	46% C, 28% G, 22% W, 04% O

For the preliminary SAR investigation, three spherical target volumes are defined in MATLAB® after the E-field simulations. As the original dielectric properties within the target volumes are kept, these targets are heterogeneous. In addition to these, two realistic test cases are considered: one in the larynx for the neck applicator and one in the meninges for the brain applicator. These targets are defined before the E-field simulations, and their volumes are filled with a homogeneous material whose properties are determined by taking the weighed average of the materials originally inside. This results in a conservative approach where the tumor does not exhibit increased conductivity. The volume and composition of the 5 targets are described in table 1 and shown in figures 5 and 6. Resulting tumor properties for the realistic cases are reported in table 2.

In all cases, the target volume is a contiguous shape, as multi-target treatment planning is beyond the scope of the present work. The artificial targets are included to evaluate the i-TR scheme's ability to achieve target coverage and HS suppression for different tumor sizes. The larynx case is included to assess the HTP's ability to target concave shapes with both superficial and deep areas. Note that the trachea lumen creates a cavity in the target volume. The meningioma is included to investigate the case where multiple polarization directions are interfering in the target volume.

3.3. E-field simulations and SAR computation

The E-field distributions of each antenna within the applicator are obtained numerically using the commercial software CST Microwave Studio® (Dassault Systèmes SE, Vélizy-Villacoublay, France 2019). The software implements an FDTD scheme on a hexahedral mesh with possibility for locally denser sampling grids. The complex geometrical curves of the SGBT antennas are sampled at $0.5/\sqrt{3}$ mm to correctly represent at any angle the 0.5 mm thick copper plate with which they are realized. The mesh resolution within the patient varies between this value and a maximum of 2 mm. Together with the water bolus, this results in $\approx 125/220$ million
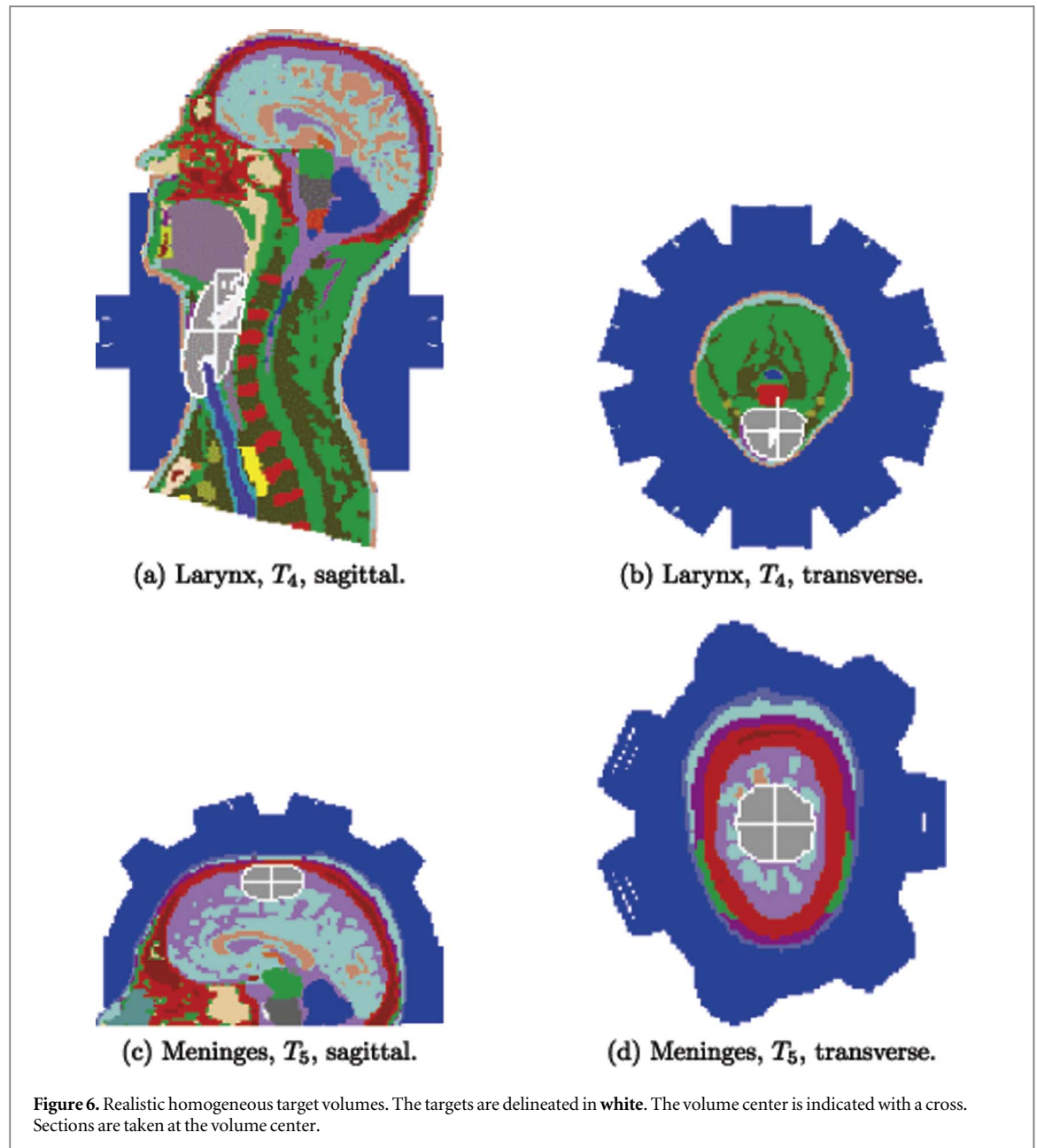
(a) Larynx, T_4, sagittal.

(b) Larynx, T_4, transverse.

(c) Meninges, T_5, sagittal.

(d) Meninges, T_5, transverse.

Figure 6. Realistic homogeneous target volumes. The targets are delineated in **white**. The volume center is indicated with a cross. Sections are taken at the volume center.

Table 2. Properties of the homogeneous materials filling the target volumes in the realistic cases, obtained as the weighed average of the original materials within the volume. Some properties are adjusted for hyperthermic conditions.

Tumor	$\epsilon\,[\sim]$	$\sigma\,(\mathrm{S\,m^{-1}})$	$\rho\,(\mathrm{kg\,m^{-3}})$	$k\,(\mathrm{W\,Km^{-1}})$	$c\,(\mathrm{K\,K^{-1}\,Kg^{-1}})$	$\omega_b\,(\mathrm{kW\,Km^{-3}})$	$Q_m\,(\mathrm{kW\,m^{-3}})$
Larynx	47.8	0.674	1088	0.423	3.285	22.033	5.456
Meninges	57.3	1.372	1063	0.535	3.754	17.048	5.478

cells for the collar/helmet setups, respectively. The almost doubled amount of mesh cells for the helmet setup is due to the antenna arrangement occupying more effectively all 3 dimensions in space. Absorbing boundary conditions (PML) are defined for all sides of the computational domain.

Upon import for post-processing in MATLAB®, the E-field distributions are re-sampled to a constant grid resolution of 2 mm. Out of these distributions, the local SAR matrices $Q_f(x, y, z)$ are constructed according to equation (4). This results in 1.1 million matrices for the neck model and 0.3 million for the brain one (considering the patient only). Each element $q_{i,j}(x, y, z)$ is further spatially averaged according to a 1g SAR mass-averaging scheme. The averaging scheme is similar to the *CST Legacy* one as described in (Qi *et al* 2008): we treat surface voxels by expanding a spherical kernel until the mass of patient tissues within reaches 1g.

3.4. Thermal simulations

To validate the HTP plans, steady-state thermal simulations are performed with CST Microwave Studio®. We consider only the realistic scenarios and only the frequency combination that yields the lowest HTQ after i-TR optimization. This combination would be the one selected for treatment after quickly surveying all possible combinations with i-TR. The thermal properties of the HSs are also taken from the IT'IS database. However, to mimic the hyperthermic stress condition of the body, the muscle's blood flow perfusion is increased by a factor 4 (Lang *et al* 1999, De Greef *et al* 2010). Moreover, the thermal conductivity of the cerebrospinal fluid is increased by a factor 10 to emulate the convective transport of heat (Schooneveldt *et al* 2019). The tumor thermal properties are calculated as a weighed average of the tissues originally composing its volume, in the same way as for the electromagnetic properties. The tumor blood perfusion rate is further diminished by a factor 0.7 to account for the chaotic vascular structure that characterizes neoplasms (Song 1984, Lang *et al* 1999). The tumor properties are summarized in table 2.

3.5. Choice of operating frequencies

The set of possible operating frequencies is constructed by stepping 100 MHz within the antenna working range 400–800 MHz, yielding the following set:

$$F = [400, 500, 600, 700, 800]^t \text{ MHz}. \tag{13}$$

Out of this set, all the single and double frequency combinations are evaluated, resulting in 15 operating frequency settings. This is to highlight potential frequency-dependent phenomena within the patient and to evaluate the i-TR scheme's robustness to different combinations of operating frequencies, while at the same time keeping the amount of test cases at a minimum.

3.6. Implementation of EV and PS

The EV implementation is similar to the one used in Guérin *et al* (2018). It determines via a direct solution the set of steering parameters that maximizes the SAR amplification factor (SAF), defined as the following quadratic ratio:
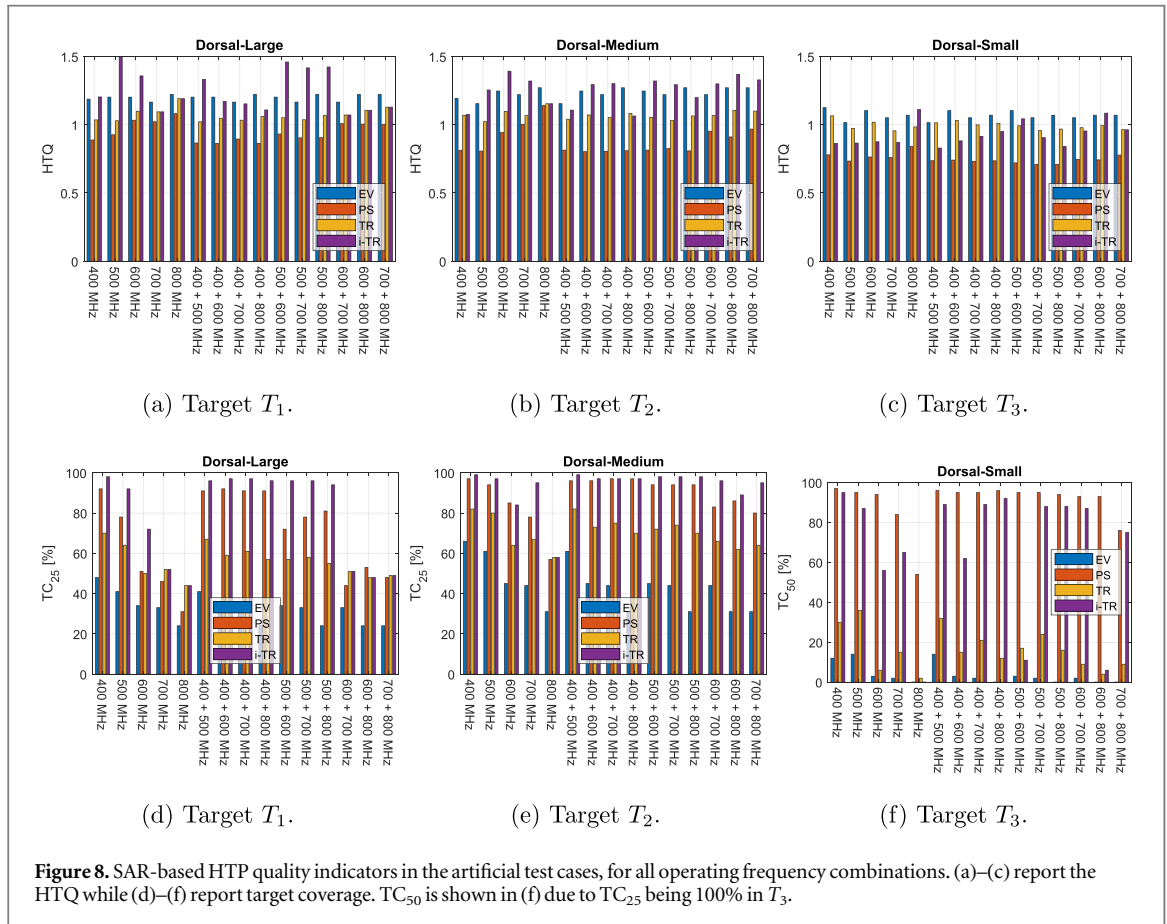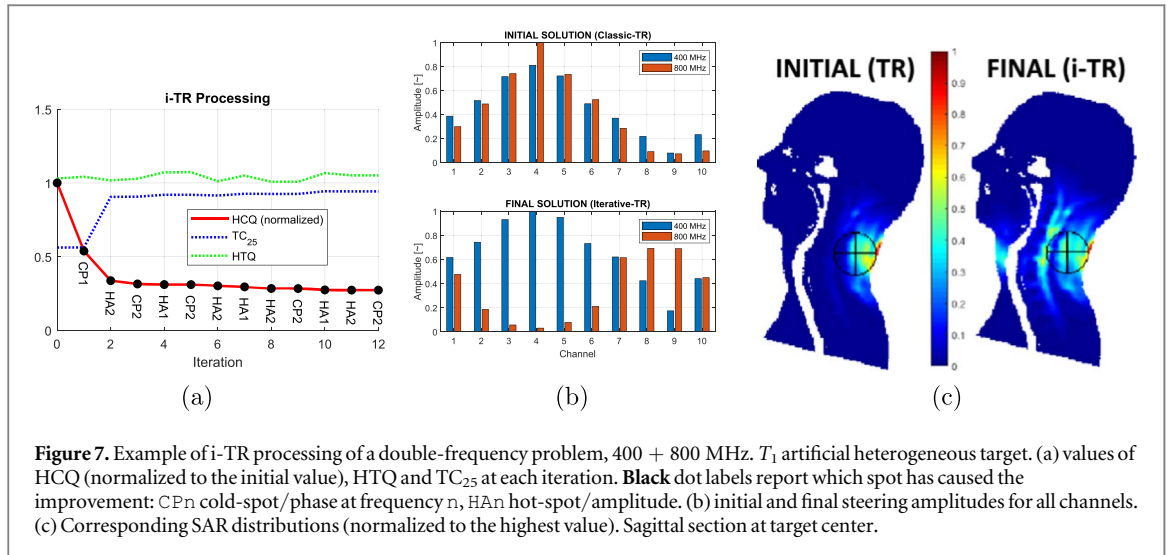
$$SAF = \frac{\overline{SAR_T}}{\overline{SAR_R}}, \tag{14}$$

where $\overline{SAR_T}$ is the average SAR in the target, and $\overline{SAR_R}$ is the average SAR in the rest. An important consequence of how equation (14) is constructed is that only one frequency at a time from any working set can maximize such ratio (Zanoli and Trefná 2020). The amplitude of the other frequencies must be set to zero, and the only active frequency is the one whose interference pattern best fits the target shape and location. This approach differs substantially from the continuous FIR solution described in Converse *et al* (2006), which, to the best of the authors' knowledge, is the only published study on wide-band EV beam-forming. Their approach is not applicable here since the spectrum is discrete. Naturally, maximizing the SAF is not the same as minimizing nonlinear indicators such as HTQ, which usually correlate better with the resulting thermal dose.

The PS implementation used for this study is the one readily available in MATLAB® (`particleswarm`). The cost function is the HTQ as described at the beginning of this section. In order for PS to properly converge regardless of the problem's complexity (Piotrowski *et al* 2020), some of its settings are made proportional to the number of variables, $n_v = 2 \cdot n_c \cdot n_f$, i.e. phase and amplitude for each channel at each frequency. In particular, the number of particles is set to $10 \cdot n_v$, and the optimization is halted when n_v consecutive iterations have produced a relative change in the objective function smaller than 0.1. Other settings have been kept to their default values. When the `particleswarm` algorithm has completed, the optimization is handed over to a local optimizer (`fmincon`) and the solution is further refined until the relative parameter change falls below 0.01, thus reaching the desired precision of 1%.
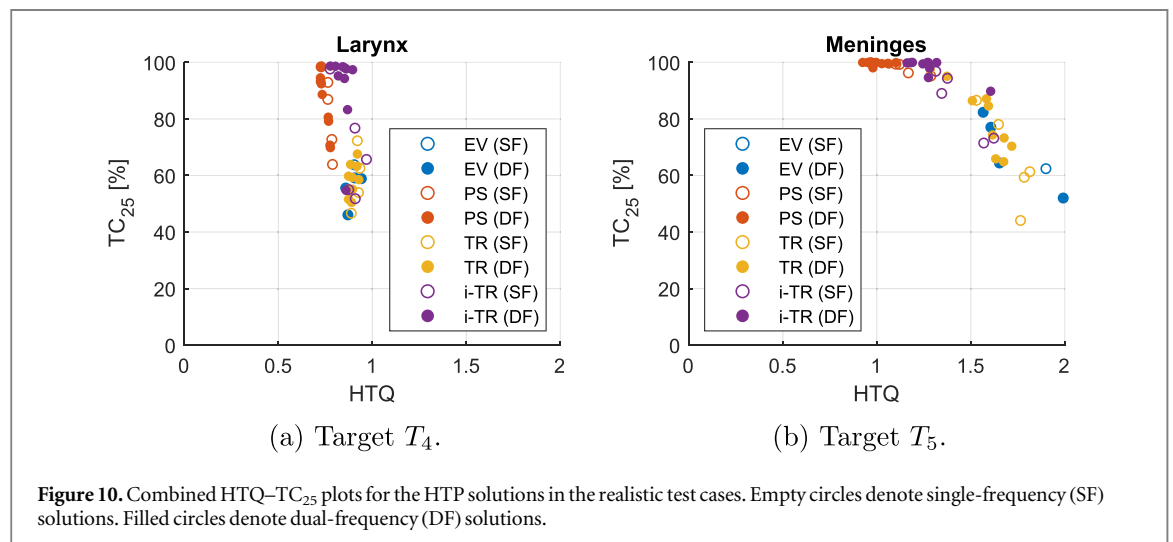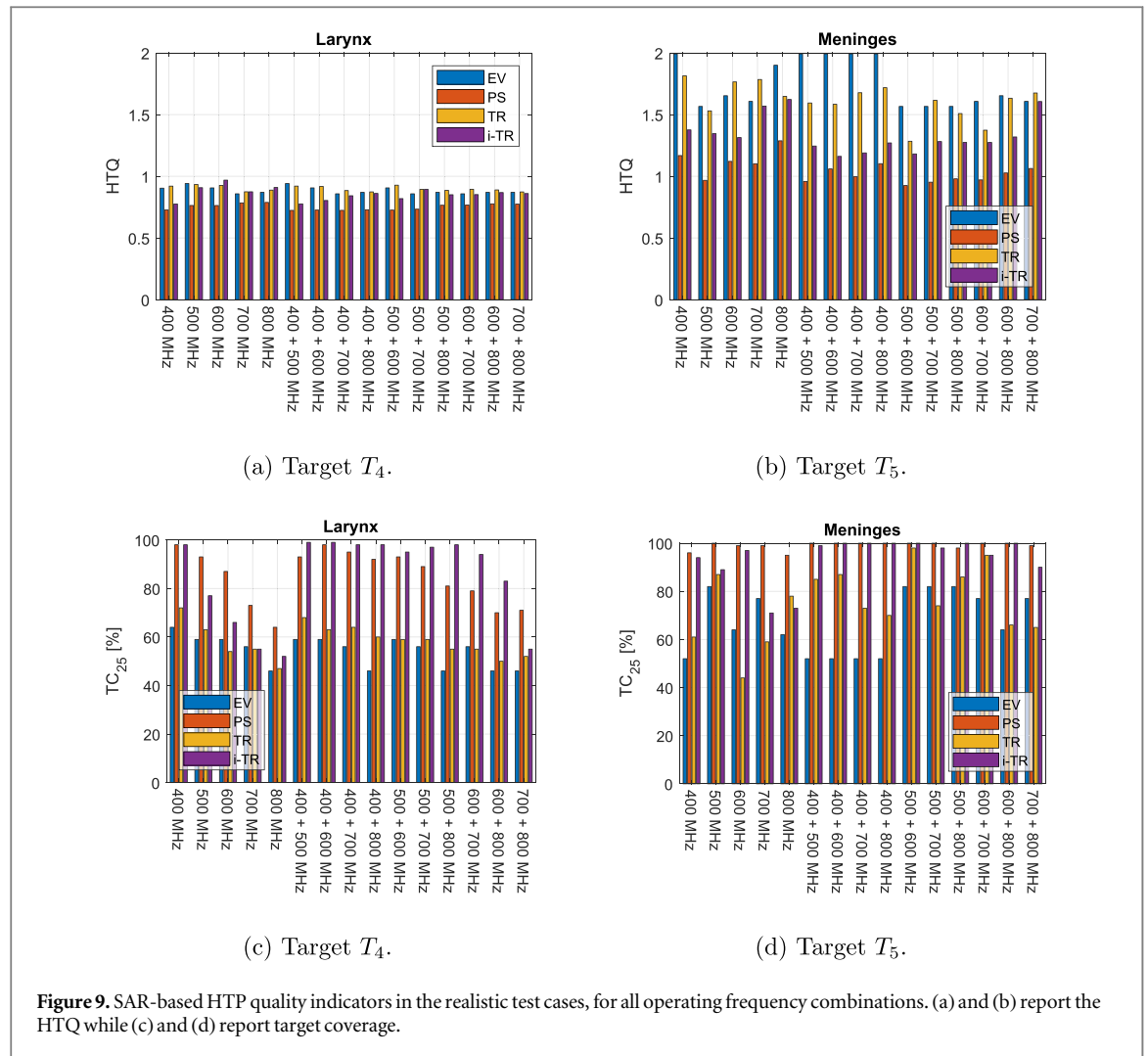
4. Results

Figure 7 shows a typical i-TR processing and its results for a representative artificial target case. Starting from the classic TR solution, the HCQ is progressively minimized until no further improvement is achieved by either cold- or HS iterations. During this process, the HTQ and TC$_{25}$ vary according to the current solution. In general, HTQ floats around the initial value, while TC$_{25}$ is strongly enhanced within a few iterations. The HCQ value is improved significantly throughout the entire process. This reflects in a more homogeneous SAR distribution within the target and in a reduction of the most relevant HS, which, in this case, is located in the skin layer adjacent to the target. The initial steering parameter amplitudes, figure 7, exhibit the typical TR pattern where each antenna radiates power proportionally to its vicinity to the target. The final amplitude settings clearly

Figure 7. Example of i-TR processing of a double-frequency problem, $400 + 800$ MHz. T_1 artificial heterogeneous target. (a) values of HCQ (normalized to the initial value), HTQ and TC_{25} at each iteration. **Black** dot labels report which spot has caused the improvement: `CPn` cold-spot/phase at frequency n, `HAn` hot-spot/amplitude. (b) initial and final steering amplitudes for all channels. (c) Corresponding SAR distributions (normalized to the highest value). Sagittal section at target center.

Figure 8. SAR-based HTP quality indicators in the artificial test cases, for all operating frequency combinations. (a)–(c) report the HTQ while (d)–(f) report target coverage. TC_{50} is shown in (f) due to TC_{25} being 100% in T_3.

demonstrate how i-TR can exploit different frequencies to cover both superficial and deeper parts of the target volume, as confirmed also by the SAR distribution in figure 7(c).

4.1. SAR evaluation

SAR-based HTP quality indicators for the artifical test cases are reported in figure 8. The lowest HTQ for any given problem and frequency combination is achieved by PS, being configured to minimize this indicator. However, this does not always translate into better coverage. The i-TR returns sensibly higher TC_{25} values in the large and medium cases, at the expense of an increase in HTQ with respect to the initial TR solution. While some solutions become impractical due to this increase, there is always at least one optimal frequency combination

Figure 9. SAR-based HTP quality indicators in the realistic test cases, for all operating frequency combinations. (a) and (b) report the HTQ while (c) and (d) report target coverage.

Figure 10. Combined HTQ–TC$_{25}$ plots for the HTP solutions in the realistic test cases. Empty circles denote single-frequency (SF) solutions. Filled circles denote dual-frequency (DF) solutions.

where i-TR achieves HTQ ≈ 1 and TC$_{25} \approx 100\%$. In the small target case, i-TR also lowers the HTQ provided by classic TR while achieving remarkably higher TC$_{50}$ values. For this target, which is less heterogeneous than T_1 and T_2 (see table 1), the solutions provided by PS and i-TR are comparable in quality. EV exhibits consistently high HTQ and poor coverage in all cases.

SAR-based HTP indicators for the realistic targets are reported in figure 9. Once more, PS returns the lowest HTQ for each case. All algorithms yield comparable HTQ values below 1 in the larynx, while only PS manages to reach values below 1 in the meninges. EV and classic TR perform similarly in the larynx case, achieving
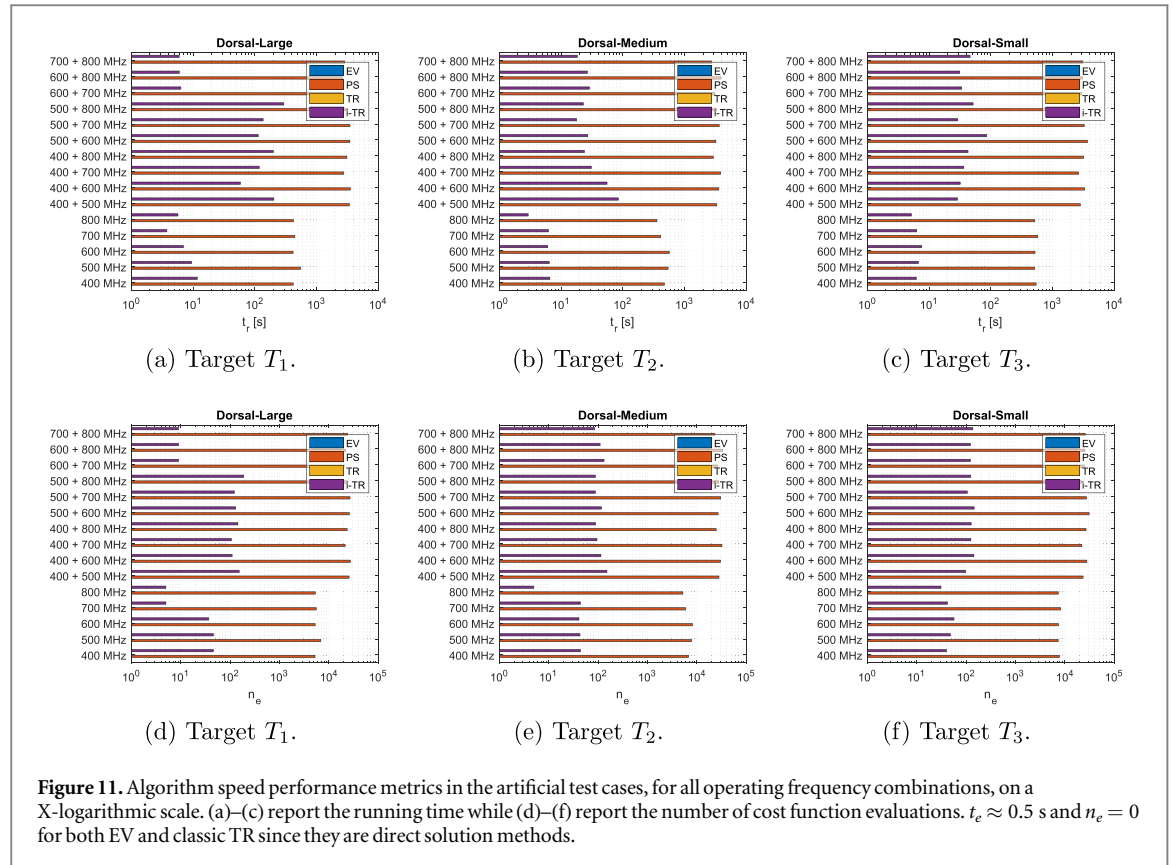
Figure 11. Algorithm speed performance metrics in the artificial test cases, for all operating frequency combinations, on a X-logarithmic scale. (a)–(c) report the running time while (d)–(f) report the number of cost function evaluations. $t_e \approx 0.5$ s and $n_e = 0$ for both EV and classic TR since they are direct solution methods.
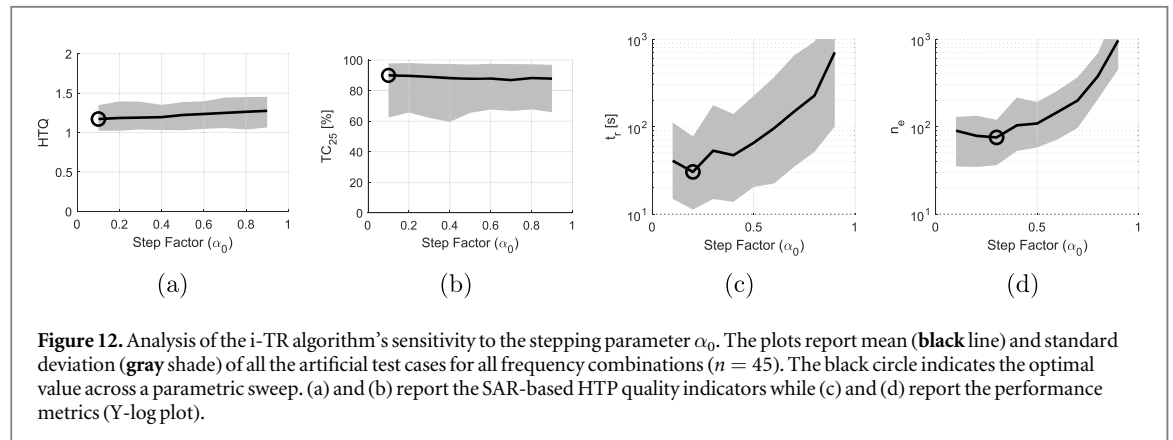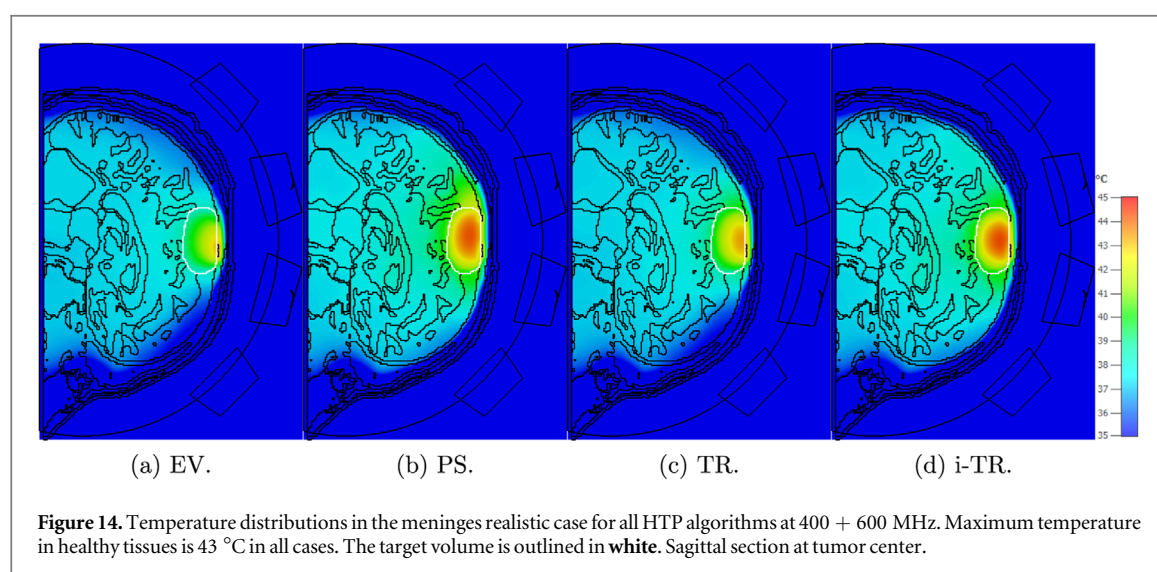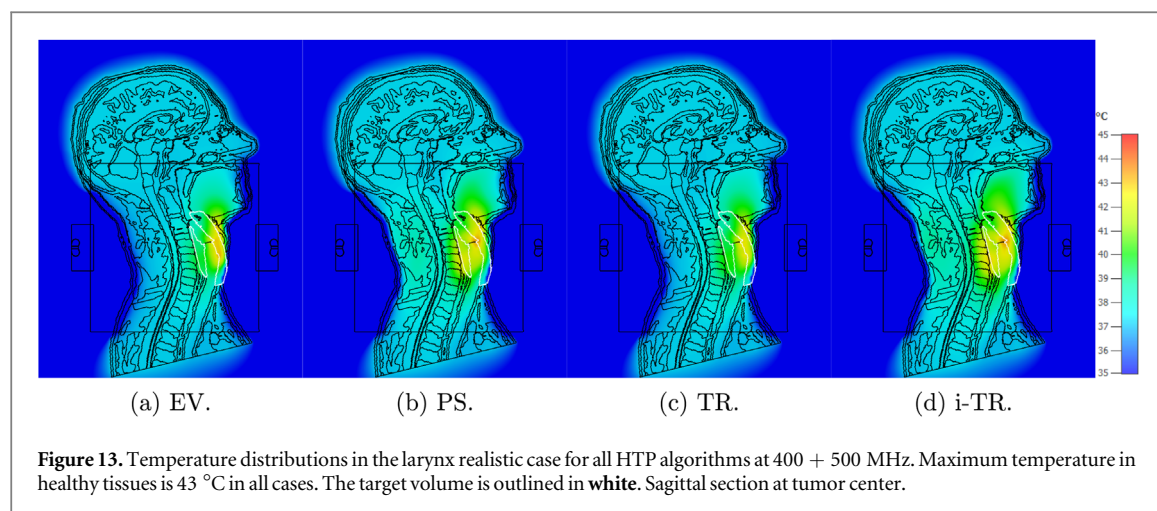

Figure 12. Analysis of the i-TR algorithm's sensitivity to the stepping parameter α_0. The plots report mean (**black** line) and standard deviation (**gray** shade) of all the artificial test cases for all frequency combinations ($n = 45$). The black circle indicates the optimal value across a parametric sweep. (a) and (b) report the SAR-based HTP quality indicators while (c) and (d) report the performance metrics (Y-log plot).

acceptable HTQ, but suboptimal coverage. EV fails to provide viable solutions for the meninges, with HTQ always above 1.5, and TC_{25} above threshold only at 500 MHz and 700 MHz. In contrast, i-TR yields HTQ values much closer to the global PS optimum for this case. More importantly, it does so with simultaneous extensive target coverage. In the larynx model, TC_{25} is often higher for i-TR than for PS when more than one frequency is considered. The SAR results for these two realistic cases are further summarized into two combined HCQ–TC_{25} plots in figure 10. In both plots, the dual-frequency solutions provided by i-TR are seen to be located near the TC_{25} optimum (100%) and close to PS's global HTQ optimum.

4.2. Performance analysis
Speed performance metrics for the artificial test cases are reported in figure 11. Since EV and TR are direct solution methods, they take less than a second to complete. About 6000 cost function evaluations are needed for PS to return a single-frequency solution, and up to 30 000 in the case of two frequencies. This translates into long execution times, with a typical run taking about 10 minutes for one frequency and 50 minutes for two frequencies. Conversely, i-TR manages to return a single-frequency solution within at most 50 evaluations, and a double-frequency solution in 100 evaluations. This reflects into at most 10 s running time in the single-

Figure 13. Temperature distributions in the larynx realistic case for all HTP algorithms at 400 + 500 MHz. Maximum temperature in healthy tissues is 43 °C in all cases. The target volume is outlined in **white**. Sagittal section at tumor center.

Figure 14. Temperature distributions in the meninges realistic case for all HTP algorithms at 400 + 600 MHz. Maximum temperature in healthy tissues is 43 °C in all cases. The target volume is outlined in **white**. Sagittal section at tumor center.

frequency case, and on average 50 seconds for a double-frequency problem. Performance metrics for the realistic cases are not reported since they indicate similar trends.

4.3. Sensitivity analysis

The results of the sensitivity analysis with respect to the initial step factor α_0 are reported in figure 12. Both HTP quality indicators exhibit negligible variations across the sweep, meaning that the solution provided by i-TR is stable in this respect. A closer look suggests that the optimum is located at the lowest end of the α_0 range. This can be intuitively explained by the fact that smaller stepping allows the algorithm to get closer to the HCQ optimum. High α_0 values exponentially increase the convergence time and computational burden of the algorithm, indicating that the initial classic TR solution is already close to the optimum and only small steps are needed to improve its HCQ value. On the other hand, both t_r and n_e tend to increase again towards $\alpha_0 = 0$, as a consequence of the step being too small to quickly reach the optimum HCQ. In conclusion, $\alpha_0 = 0.1$ seems to be an appropriate value for this parameter.

4.4. Thermal validation

Figures 13 and 14 show the thermal distributions for the realistic cases. It can be seen that both direct solvers, EV and TR, fail to reach therapeutic temperatures in the deeper parts of the tumors. In the larynx case, the trachea acts as a heat barrier between opposing sides of the target volume, whose morphology is toroidal. PS and i-TR manage to overcome this barrier by extending the SAR coverage to the inner side, at the expense of higher average temperatures in the healthy tissues. This higher power deposition, however, does not result in additional HSs. i-TR performs better in this sense than PS by gaining half a degree in median temperature, see table 3. For the meningioma, both EV and TR end up maximizing the peak SAR in the target which results in a focal spot close to the skull. This spot is however mitigated by the cooling effect of the bolus, so that neither high peak
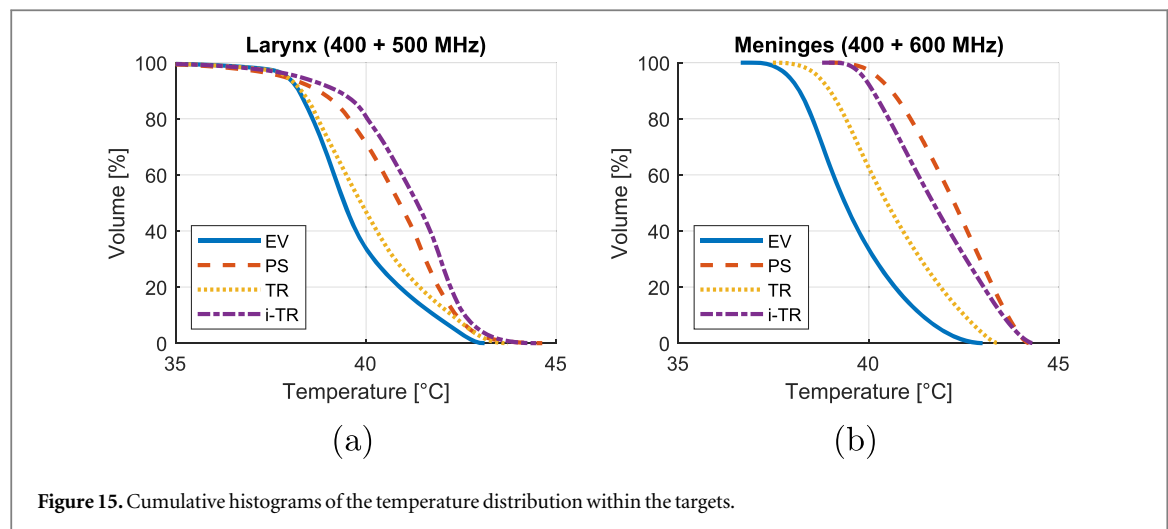
Figure 15. Cumulative histograms of the temperature distribution within the targets.

Table 3. Median temperatures (T_{50}) reached inside the target volume in each of the thermal test cases for all HTP algorithms. Values in °C.

Tumor	EV	PS	TR	i-TR
Larynx	39.43	40.87	39.87	41.34
Meninges	39.37	42.24	40.47	41.69

temperatures nor sufficient coverage are achieved within the target. Both PS and i-TR shift this main SAR peak deeper in the brain, reaching high median temperatures. i-TR closely follows PS by only half a degree lower T_{50}. These results are further illustrated in the cumulative histograms, figure 15.

5. Discussion

Hyperthermia requires an optimal SAR distribution in the patient in terms of raw target power deposition, target coverage, and HS suppression in healthy tissues. Target SAR coverage has in fact been shown to be predictive for the therapeutic outcome of the treatment (Myerson *et al* 1990, Lee *et al* 1998). To improve on these aspects, the HTQ and the TCx indicators have been proposed and shown to be effective when applied retrospectively to clinical data sets (Paulides *et al* 2016, Bellizzi *et al* 2019). However, HTQ and TC$_x$ are two different cost functions whose optimal distributions do not coincide. In particular, a single-frequency HTP might yield acceptable HTQ, but poor target coverage. This effect is apparent in figures 8 and 9: even when the HTQ closely fluctuates around 1, the TC$_x$ exhibits a strong frequency-dependent trend, quickly falling below the acceptance threshold. To satisfy both HTQ < 1 and TC$_x > 75\%$, one must carefully select the optimal operating frequency, which depends on the applicator in use, the patient's anatomy, and the target shape. For the larynx case used in this study, the optimal frequency lies around 400 MHz, while for the meninges 500 MHz appears to be a better choice. This motivates the need for wide-band applicators and for treatment planning tools capable of seeking the best treatment frequency within the available band. Figures 8 and 9 further show that in a multi-frequency setting, the requirements on the HTQ and TC$_x$ can be more easily fulfilled when two frequencies are selected simultaneously. In other words, the multi-frequency approach helps reaching the multiple objectives needed for a successful hyperthermia dose delivery.

The proposed i-TR technique aims at quickly determining such an overall optimal SAR distribution by exploiting the different frequency components to minimize a custom cost function, the HCQ. This cost function is designed to reach the multiple objectives above while enabling a TR-based iterative approach. The SAR-based results, section 4.1, suggest that the method is successful in finding viable solutions for a given problem, independently of the target's size, location, morphology or composition. They further indicate that the method is robust to problems involving mixed polarization axes. The quality of the i-TR solution can depend on the selected set of operating frequencies, however the high execution speed makes it possible to evaluate all frequency combinations and always determine one viable solution. Note that this solution might not be the global optimum in terms of HCQ. We further point out that, although there is no guarantee of improvement of

an initial TR solution by i-TR, the process is stable as it can never return a solution worse than the initial one in terms of HCQ.

The thermal validation, section 4.4, fundamentally confirms the i-TR's ability to provide viable HTP solutions and further emphasizes the difference in HTQ and TC_x as treatment planning goals. In the larynx case, for instance, all HTP algorithms exhibit similar HTQ values below 1 at the selected frequency combination. However, only for i-TR and PS this translates into high thermal doses, thanks to their higher SAR coverage. EV and classic TR fail to fully exploit the applicator's heating capabilities, falling short of 2 °C on average in T_{50} for the two cases. The small improvement in HTQ brought about by PS, negligible at a first glance, results in a significantly higher median tumor temperature. It is however i-TR to perform best in the larynx, with half a degree higher T_{50} than PS. This is likely due to the compromise that HCQ seeks between low HTQ and high coverage. In the meninges, the situation is similar for EV and TR, while i-TR provides again a solution very close to PS, with only half a degree lower T_{50}. While it is not possible to draw general conclusions about the relationship between HTQ, TC_x, HCQ and the resulting temperature distribution due to the limited amount of test cases, the thermal validation indicates that the HTP solutions provided by i-TR can be considered as clinically relevant.

Regarding EV, many improvements have been suggested over the years in an effort to exploit this extremely fast solution method. Works such as those of Köhler *et al* (2001) and Mestrom *et al* (2014) apply weighing functions to the SAR distribution in order to reduce the SAR peak in the healthy tissues and improve the SAR homogeneity within the target. The weight distribution itself, however, needs to be determined by means of an iterative procedure. Moreover, these modifications only apply to the single-frequency scenario. In a multi-frequency setting, the fundamental single-frequency limitation of the EV cost function ($\overline{SAR}_T / \overline{SAR}_R$) needs to be resolved to fully exploit the treatment capabilities of wide-band applicators (Zanoli and Trefná 2020). Recently, an emerging time- and frequency-multiplexed beam-forming method has been proposed by Kuehne *et al* (2020). The method is based on quadratic programming (QP) and is therefore extremely fast in determining the optimal set of frequencies, steering parameters and temporal sequences that best approximate a specified SAR pattern. However, the method does not determine the optimal SAR pattern in itself. While this is a very powerful approach, we believe that a relevant comparison between applicators should be grounded on clinically relevant HTP quality indicators, such as HTQ and TC_x. These have been shown to correlate with high tumor temperatures (Bellizzi *et al* 2019), which are the ultimate goal in hypethermia. However, since these indicators involve a nonlinear step, they cannot be solved for with fast QP-based algorithms.

The proposed i-TR technique runs in nearly real-time even in the case of high-resolution model matrices such as those considered in this study. The 2 mm resolution is necessary to model the thin anatomical features of the vertebrae and the skull, which strongly affect the wave propagation. Current clinical HTP tools for online complaint-adaptive steering use coarse resolutions of 5 mm for 70 MHz and 434 MHz applicators to be able to quickly recompute the steering parameters (Rijnen *et al* 2013, Kok *et al* 2017). For UWB applicators utilizing frequencies up to 800 MHz, this resolution is no longer sufficient, especially when considering tumors in the brain.

We point out that the proposed i-TR technique differs substantially from the iterative TR method developed by Montaldo and colleagues for ultrasound applications (Montaldo *et al* 2004). In HIFU, the aim is to restore the sharp TR focal spot after distortions caused by lossy and heterogeneous media. In MW-HT, the problem faced is the opposite: to de-focus the sharp SAR peak caused by TR in order to achieve better coverage across the whole target volume. As a final consideration, we note that the i-TR implementation described in this paper is not unique. For example, the *cold-spot → HS* order in the iterative scheme, figure 3, could be swapped. Similarly, the identification of hot- and cold-spots could be performed right before each spot iteration, as done here, or only once before both iterations. During internal tests, we could not identify any major effects of these choices on the HTP outcome.

6. Conclusion

The proposed i-TR beam-forming technique is shown to deliver HTP solutions equivalent to those provided by global optimizers such as PS, while being orders of magnitude faster. Results indicate that the method is robust to different array and target configurations. The custom HCQ cost function solved for by the iterative method leads to solutions that exhibit a good compromise between raw power deposition in the tumor, HS suppression in healthy tissues, and target coverage even in deeper regions. Overall, the described i-TR technique provides the means for fast comparisons of a large number of potential array configurations and frequency combinations to optimally treat a given patient. In a clinical setting, i-TR might be further extended for use as a real-time steering parameter re-optimization procedure upon localized complaint from the patient.

Acknowledgments

ORCID iDs

Massimiliano Zanoli ⬤ https://orcid.org/0000-0002-3149-6905
Hana Dobšíček Trefná ⬤ https://orcid.org/0000-0001-6025-0819

References

Bardati F, Borrani A, Gerardino A and Lovisolo G A 1995 SAR optimization in a phased array radiofrequency hyperthermia system *IEEE Trans. Biomed. Eng.* **42** 1201–7

Battaglia G, Morabito A, Palmeri R and Isernia T 2020 Constrained focusing of vector fields intensity in near zone and/or complex scenarios as a low-dimensional global optimization *J. Electromagn. Waves Appl.* **34** 1977–89

Bellizzi G G, Crocco L, Battaglia G M and Isernia T 2017 Multi-frequency constrained SAR focusing for patient specific hyperthermia treatment *IEEE J. Electromagn. RF Microwaves Med. Biol.* **1** 74–80

Bellizzi G G, Drizdal T, van Rhoon G C, Crocco L, Isernia T and Paulides M M 2019 Predictive value of sar based quality indicators for head and neck hyperthermia treatment quality *Int. J. Hyperth.* **36** 455–64

Böhm M, Kremer J and Louis A 1993 Efficient algorithm for computing optimal control of antennas in hyperthermia *Surv. Math. Ind.* **3** 233–51

Canters R A, Paulides M M, Franckena M F, van der Zee J and van Rhoon G C 2012 Implementation of treatment planning in the routine clinical procedure of regional hyperthermia treatment of cervical cancer: an overview and the Rotterdam experience *Int. J. Hyperth.* **28** 570–81

Canters R, Franckena M, van der Zee J and Van Rhoon G 2010 Optimizing deep hyperthermia treatments: are locations of patient pain complaints correlated with modelled SAR peak locations? *Phys. Med. Biol.* **56** 439–51

Canters R, Paulides M, Franckena M, Mens J and Van Rhoon G 2013 Benefit of replacing the sigma-60 by the sigma-eye applicator *Strahlentherapie und Onkologie* **189** 74–80

Canters R, Wust P, Bakker J and Van Rhoon G 2009 A literature survey on indicators for characterisation and optimisation of SAR distributions in deep hyperthermia, a plea for standardisation *Int. J. Hyperth.* **25** 593–608

Cihoric N *et al* 2015 Hyperthermia-related clinical trials on cancer treatment within the ClinicalTrials.gov registry *Int. J. Hyperth.* **31** 609–14

Converse M, Bond E J, Veen B and Hagness C 2006 A computational study of ultra-wideband versus narrowband microwave hyperthermia for breast cancer treatment *IEEE Trans. Microwave Theory Tech.* **54** 2169–80

Dassault Systèmes SE, Vélizy-Villacoublay, France 2019 CST Studio Suite 2019

Datta N, Ordóñez S G, Gaipl U, Paulides M, Crezee H, Gellermann J, Marder D, Puric E and Bodis S 2015 Local hyperthermia combined with radiotherapy and-/or chemotherapy: recent advances and promises for the future *Cancer Treat. Rev.* **41** 742–53

Datta N R, Rogers S, Ordóñez S G, Puric E and Bodis S 2016 Hyperthermia and radiotherapy in the management of head and neck cancers: a systematic review and meta-analysis *Int. J. Hyperth.* **32** 31–40

De Greef M, Kok H, Correia D, Bel A and Crezee J 2010 Optimization in hyperthermia treatment planning: the impact of tissue perfusion uncertainty *Med. Phys.* **37** 4540–50

Elming P B, Sørensen B S, Oei A L, Franken N A, Crezee J, Overgaard J and Horsman M R 2019 Hyperthermia: the optimal treatment to overcome radiation resistant hypoxia *Cancers* **11** 60

Fatehi D, Van Der Zee J, Notenboom A and van Rhoon G C 2007 Comparison of intratumor and intraluminal temperatures during locoregional deep hyperthermia of pelvic tumors *Strahlentherapie und Onkologie* **183** 479–86

Fink M, Montaldo G and Tanter M 2004 Time reversal acoustics *IEEE Ultrasonics Symp., 2004,* vol 2 (Piscataway, NJ: IEEE) pp 850–9

Gavazzi S, van Lier A L, Zachiu C, Jansen E, Lagendijk J J W, Stalpers L J A, Crezee H and Kok H P 2020 Advanced patient-specific hyperthermia treatment planning *Int. J. Hyperth.* **37** 992–1007

Gosselin M-C *et al* 2014 Development of a new generation of high-resolution anatomical models for medical device evaluation: the Virtual Population 3.0 *Phys. Med. Biol.* **59** 5287–303

Guérin B, Villena J F, Polimeridis A G, Adalsteinsson E, Daniel L, White J K, Rosen B R and Wald L L 2018 Computation of ultimate SAR amplification factors for radiofrequency hyperthermia in non-uniform body models: impact of frequency and tumour location *Int. J. Hyperth.* **34** 87–100

Guo B, Xu L and Li J 2005 Time reversal based microwave hyperthermia treatment of breast cancer *Microwave Opt. Technol. Lett.* **47** 335–8

Hasgall P, Neufeld E, Gosselin M, Klingenböck A, Kuster N, Hasgall P and Gosselin M 2012 IT'IS database for thermal and electromagnetic parameters of biological tissues Version 4.0 (15 May 2018) (https://doi.org/10.13099/VIP21000-04-0. itis.swiss/database)

Iero D A, Crocco L, Isernia T and Korkmaz E 2016 Optimal focused electromagnetic hyperthermia treatment of breast cancer *2016 10th European Conf. on Antennas and Propagation (EuCAP)* (Piscataway, NJ: IEEE) pp 1–2

Köhler T, Maass P, Wust P and Seebass M 2001 A fast algorithm to find optimal controls of multiantenna applicators in regional hyperthermia *Phys. Med. Biol.* **46** 2503–14

Kok H P, Gellermann J, van den Berg C A, Stauffer P R, Hand J W and Crezee J 2013 Thermal modelling using discrete vasculature for thermal therapy: a review *Int. J. Hyperth.* **29** 336–45

Kok H P, Korshuize-van Straten L, Bakker A, de Kroon-Oldenhof R, Geijsen E D, Stalpers L J and Crezee J 2017 Online adaptive hyperthermia treatment planning during locoregional heating to suppress treatment-limiting hot spots *Int. J. Radiat. Onco. Biol.Phys.* **99** 1039–47

Kok H, Wust P, Stauffer P R, Bardati F, Van Rhoon G and Crezee J 2015 Current state of the art of regional hyperthermia treatment planning: a review *Radiat. Oncol.* **10** 196

Kuehne A, Oberacker E, Waiczies H and Niendorf T 2020 Solving the time-and frequency-multiplexed problem of constrained radiofrequency induced hyperthermia *Cancers* **12** 1072

Lang J, Erdmann B and Seebass M 1999 Impact of nonlinear heat transfer on temperature control in regional hyperthermia *IEEE Trans. Biomed. Eng.* **46** 1129–38

Leduc N, Okita K, Sugiyama K, Takagi S and Matsumoto Y 2012 Focus control in HIFU therapy assisted by time-reversal simulation with an iterative procedure for hot spot elimination *J. Biomech. Sci. Eng.* **7** 43–56

Lee H K, Antell A G, Perez C A, Straube W L, Ramachandran G, Myerson R J, Emami B, Molmenti E P, Buckner A and Lockett M A 1998 Superficial hyperthermia and irradiation for recurrent breast carcinoma of the chest wall: prognostic factors in 196 tumors *Int. J. Radiat. Oncol. Biol. Phys.* **40** 365–75

Lerosey G, De Rosny J, Tourin A, Derode A, Montaldo G and Fink M 2004 Time reversal of electromagnetic waves *Phys. Rev. Lett.* **92** 193904

Mestrom R, Van Engelen J, Van Beurden M, Paulides M, Numan W and Tijhuis A 2014 A refined eigenvalue-based optimization technique for hyperthermia treatment planning *The 8th European Conf. on Antennas and Propagation (EuCAP 2014)* (Piscataway, NJ: IEEE) pp 2010–3

Montaldo G, Tanter M and Fink M 2004 Real time inverse filter focusing through iterative time reversal *J. Acoust. Soc. Am.* **115** 768–75

Myerson R J, Perez C A, Emami B, Straube W, Kuske R R, Leybovich L and Von Gerichten D 1990 Tumor control in long-term survivors following superficial hyperthermia *Int. J. Radiat. Oncol. Biol. Phys.* **18** 1123–9

Paulides M, Bakker J, Linthorst M, Van der Zee J, Rijnen Z, Neufeld E, Pattynama P, Jansen P, Levendag P and Van Rhoon G 2010 The clinical feasibility of deep hyperthermia treatment in the head and neck: new challenges for positioning and temperature measurement *Phys. Med. Biol.* **55** 2465–80

Paulides M, Bakker J, Neufeld E, Zee J V D, Jansen P, Levendag P and Van Rhoon G 2007 The HYPERcollar: a novel applicator for hyperthermia in the head and neck *Int. J. Hyperth.* **23** 567–76

Paulides M M, Stauffer P R, Neufeld E, Maccarini P F, Kyriakou A, Canters R A, Diederich C J, Bakker J F and Van Rhoon G C 2013 Simulation techniques in hyperthermia treatment planning *Int. J. Hyperth.* **29** 346–57

Paulides M M, Verduijn G M and Van Holthe N 2016 Status quo and directions in deep head and neck hyperthermia *Radiat. Oncol.* **11** 21

Paulides M, Trefna H D, Curto S and Rodrigues D 2020 Recent technological advancements in radiofrequency-and microwave-mediated hyperthermia for enhancing drug delivery *Adv. Drug Deliv. Rev.* **163–164** 3–18

Piotrowski A P, Napiorkowski J J and Piotrowska A E 2020 Population size in particle swarm optimization *Swarm Evolutionary Comput.* **58** 100718

Qi N, Zhang M, Wittig T and Prokop A 2008 Application of CST time domain algorithm in the electromagnetic simulation standard of the SAR for mobile phone *2008 Int. Conf. on Microwave and Millimeter Wave Technology* vol 4 (Piscataway, NJ: IEEE) pp 1717–20

Rijnen Z, Bakker J F, Canters R A, Togni P, Verduijn G M, Levendag P C, Van Rhoon G C and Paulides M M 2013 Clinical integration of software tool vedo for adaptive and quantitative application of phased array hyperthermia in the head and neck *Int. J. Hyperth.* **29** 181–93

Schooneveldt G, Trefná H D, Persson M, De Reijke T M, Blomgren K, Kok H P and Crezee H 2019 Hyperthermia treatment planning including convective flow in cerebrospinal fluid for brain tumour hyperthermia treatment using a novel dedicated paediatric brain applicator *Cancers* **11** 1183

Song C W 1984 Effect of local hyperthermia on blood flow and microenvironment: a review *Cancer Res.* **44** 4721s–30s

Takook P, Persson M, Gellermann J and Trefná H D 2017 Compact self-grounded bow-tie antenna design for an UWB phased-array hyperthermia applicator *Int. J. Hyperth.* **33** 387–400

Takook P, Persson M and Trefná H D 2018 Performance evaluation of hyperthermia applicators to heat deep-seated brain tumors *IEEE J. Electromagn. RF Microwaves Med. Biol.* **2** 18–24

Takook P, Trefná H D, Fhager A and Persson M 2015 Evaluation of the 3D time reversal method for hyperthermia treatment planning in head and neck tumors *2015 9th European Conf. on Antennas and Propagation (EuCAP)* (Piscataway, NJ: IEEE) pp 1–5

Takook P, Trefná H D, Zeng X, Fhager A and Persson M 2017 A computational study using time reversal focusing for hyperthermia treatment planning *Prog. Electromagn. Res.* **73** 117–30

The MathWorks Inc. 2019 MATLAB R2019 (Natick, MA: The MathWorks Inc.)

Thomas J-L and Fink M A 1996 Ultrasonic beam focusing through tissue inhomogeneities with a time reversal mirror: application to transskull therapy *IEEE Trans. Ultrason. Ferroelectr. Freq. Control* **43** 1122–9

Togni P, Rijnen Z, Numan W, Verhaart R, Bakker J, Van Rhoon G and Paulides M 2013 Electromagnetic redesign of the HYPERcollar applicator: toward improved deep local head-and-neck hyperthermia *Phys. Med. Biol.* **58** 5997–6009

Trefná H D, Martinsson B, Petersson T, Renström N, Torstensson M, Ravanis J, Kok P and Persson M 2017 Multifrequency approach in hyperthermia treatment planning: impact of frequency on SAR distribution in head and neck *2017 11th European Conf. on Antennas and Propagation (EUCAP)* (Piscataway, NJ: IEEE) pp 3710–2

Trefná H D, Togni P, Shiee R, Vrba J and Persson M 2012 Design of a wideband multi-channel system for time reversal hyperthermia *Int. J. Hyperth.* **28** 175–83

Trefná H D, Vrba J and Persson M 2010a Evaluation of a patch antenna applicator for time reversal hyperthemia *Int. J. Hyperth.* **26** 185–97

Trefná H D, Vrba J and Persson M 2010b Time-reversal focusing in microwave hyperthermia for deep-seated tumors *Phys. Med. Biol.* **55** 2167–85

Winter L, Oezerdem C, Hoffmann W, van de Lindt T, Periquito J, Ji Y, Ghadjar P, Budach V, Wust P and Niendorf T 2015 Thermal magnetic resonance: physics considerations and electromagnetic field simulations up to 23.5 Tesla (1 ghz) *Radiat.Oncol.* **10** 1–12

Wust P, Fähling H, Helzel T, Kniephoff M, Wlodarczyk W, Mönich G and Felix R 1998 Design and test of a new multi-amplifier system with phase and amplitude control *Int. J. Hyperth.* **14** 459–77

Yarmolenko P S, Moon E J, Landon C, Manzoor A, Hochman D W, Viglianti B L and Dewhirst M W 2011 Thresholds for thermal damage to normal tissues: an update *Int. J. Hyperth.* **27** 320–43

Zanoli M and Trefná H D 2020 Suitability of eigenvalue beam forming for discrete multi-frequency hyperthermia treatment planning *Med. Phys.* submitted